Shear loading dominated damage mechanisms and strain localization studied by in situ 3D laminography imaging and Digital Volume Correlation for AA2198-T8

Ante Buljac, Xiang Kong, Lukas Helfen, François Hild, Thilo F. Morgeneyer

Shear loading dominated damage mechanisms and strain localization studied by in situ 3D laminography imaging and Digital Volume Correlation for AA2198-T8

Ante Buljac[a,b], Xiang Kong[a], Lukas Helfen[c,d], François Hild[b], Thilo F. Morgeneyer[a,*]

[a] *MINES Paris, PSL University, Centre des Matériaux, CNRS UMR 7633, BP 87, 91003 Evry, France*
[b] *Université Paris-Saclay, CentraleSupélec, ENS Paris-Saclay, CNRS LMPS–Laboratoire de Mécanique Paris-Saclay, Gif-sur-Yvette, France*
[c] *Institute for Photon Science and Synchrotron Radiation Karlsruhe Institute of Technology (KIT), 76131 Karlsruhe, Germany*
[d] *Institut Laue–Langevin, Grenoble Cedex, 38043, France*

Abstract

Damage and strain changes during shear dominated loading were assessed *in situ* via synchrotron laminography. In combination with digital volume correlation (DVC), local strain fields inside the material were determined thanks to the contrast provided by intermetallic particles. Testing was performed on a thin sheet sample with an optimized geometry that induces shear stress states in two ligaments opposite to each other with respect to the loading axis. Examining one of the ligaments, the strain fields in the material showed the expected localization in the shear plane with a central peak in shear strain. The Lode parameter fields associated with incremental strain measurements were determined for the analyzed zone and found to be close to zero. The total Hencky von Mises strain close to failure was measured in the material bulk and reached values between 0.6 and 0.7 for a DVC element length of 20 µm. In the shear zone, damage onset in the form of grain-related elongated cracks and of voids nucleating on intermetallic particles was detected from about half of the maximum value of the equivalent strain to failure onward. Voids between particle clusters grew in shear as the particles were rigid and mostly brittle. Damage was mainly concentrated in the gage section subjected to shear and away from free surfaces, in particular away from the notches. It was characterized and quantified with respect to the maximum equivalent strain

DOI:/10.1016/j.mechmat.2023.104558

found inside the band.

Keywords: Aluminum alloy, Ductile damage, Shear loading, Tomography, Digital Volume Correlation (DVC)

1. Introduction/Motivation

Only recently, deformation and failure at lower levels of stress triaxiality, i.e., less than 1, have been actively considered in the literature. In such cases, complex non-monotonic relationships between strain at fracture and stress triaxiality have been reported [1]. The definition and measurement of fracture strains in these circumstances are difficult due to highly localized final failure location and processes [2]. In particular, the definition and choice of the measurement length, i.e. subset size in DIC, has a major effect on the result. E.g. Kahameneh et al. [3] observed that shear fracture strains reported by DIC for a DP steel are significantly affected by the employed DIC parameters, in particular the virtual strain gauge length.

The Lode parameter [4] has been identified as a suitable additional mechanical parameter to describe the mechanical loading condition and, in particular, the state of generalized shear where the Lode parameter vanishes. The Lode parameter is generally calculated from to the stress tensor, but it can also be applied to the strain rate tensor, as suggested in Lode's work [4]. Rather phenomenological models considering strain, stress triaxiality and Lode parameter have been used to try to find experimental results [1].

It has been identified that for Lode parameters of nearly zero in the gauge region of simple shear tests corresponds to principal strains that are equal and opposite assuming thickness strain is negligible. It is established that for BCC and FCC materials principal strains under simple shear deformation are equal and opposite [5]. This has also been verified experimentally in [6].

*Corresponding author.
Email address: thilo.morgeneyer@minesparis.psl.eu (Thilo F. Morgeneyer)

There are different ways in which a local shear stress state can be generated. Tubular specimens seem to be a good choice to deform materials up to fracture under a shear stress states [2, 7]. For sheet materials, flat samples need to be used. For the recrystallized AA2198 T8 alloy of the present study, a sample geometry with two ligaments under shear has been optimized [8]. The original geometry of the sample [9, 10] had some drawbacks. Single ligament shear samples may also be used [11] but failure from sample notches needs to be avoided by optimizing the sample geometry for the ductility level and strain hardening.

Ductile damage mechanisms under monotonic low stress triaxiality loading are less clear than under high stress triaxiality loading that is associated with void nucleation, growth and coalescence. Void growth is very limited under shear as the stress triaxiality is close to zero. Gross and Ravi-Chandar [12] investigated the deformation and failure of Al 6061-T6 under shear loading via *in situ* SEM. They found that second phase particles were broken, debonded or rotated. Incipient voids had minimal influence on the deformation of this material under shear. Achouri et al. [13] found for an HSLA steel that voids nucleated on the particle-steel interface, later rotated and elongated with increasing shear strain. These surface observations were subject to surface preparation artifacts and free surface effects such as the onset of surface roughness during straining.

With recent advances in synchrotron three-dimensional (3D) imaging, damage inside the material bulk was studied both qualitatively and quantitatively *in situ* [14, 15, 16, 17]. Synchrotron laminography is suited to image regions of interest in large flat samples at micrometer resolution [18, 19, 20, 21], thereby ensuring relevant mechanical conditions in the bulk of the material compared to surface observations. Basic failure mechanism at low triaxiality (i.e., shear) have been explored [22, 6] with this non-destructive 3D imaging technique. Roth et al. [22] observed void nucleation and growth on rigid hard particles in ferrite-bainite steel under shear-dominant loading. The authors validated shear damage nucleation from rigid particles, growth and rotation by a 2D finite element simulation. Voids nucleated due

to particle-matrix debonding, subsequently elongated and aligned with the major principal strain direction. Tancogne-Dejean et al. [6] observed and followed statistically intermetallic particles and pre-existing voids under low stress triaxiality proportional shear loading for a ductile Al AA2024-T3 alloy. It was found that intermetallic particles broke with cracks normal to the major principal stress direction. Pre-existing voids were shown to rotate and close. Kong et al. [23] studied damage during a 'shear to tension' loading path change for the material of the present study. It was found that damage nucleated under shear and grew on under tensile loading. It was found in Ref. [24] that increased intermetallic particle content reduced the ductility in shear for a 6XXX series alloy.

Using 3D *in situ* images, strains inside the material can be assessed if natural image contrast caused by the material microstructure, e.g., intermetallic particles, is sufficient. Digital volume correlation has been successfully applied to aluminium alloys [25, 26, 27]. 2D image correlation of projected 3D data may be an alternative method when the contrast in the 3D image is low [27, 22, 6, 28, 23].

The material employed herein is one of the third generation Al-Cu-Li alloys with higher copper over lithium ratio compared to the second generation [29, 27]. More precisely, the fuselage sheet alloy AA2198 in T851 temper (i.e., solutionized, stretched and artificially aged) was used in its recrystallized state [26, 30]. The alloy had an optimized and attractive balance of tensile strength (500 MPa in the rolling direction) and toughness among this class of third generation alloys (e.g., 2098T8 aluminum alloy) [29], and showed good properties after friction stir welding [31]. Its failure mechanisms were identified as intergranular and transgranular [26, 32]. Sub micrometer dimples were found in the slant fractured zones.

The motivation of the present analysis on shear specimen was to conduct DVC registrations in cases with high plastic strain levels and to test the ability of measuring Lode parameter fields in the shear band expressed in terms of both incremental and cumulated strain. The paper is structured as follows. The experimental setup and material properties

are first introduced. The basic principles of DVC together with the strain definition and uncertainty assessments are outlined next. The results are finally discussed. The focus is put on incremental strain activity and damage mechanisms in the monitored shear zone.

2. Experimental methods

2.1. Laminography

Synchrotron laminography [18, 33] was used for 3D imaging local regions of interest inside sheet materials under applied loading conditions. A testing device placed on the laminographic rotation stage applies the load by manually controlling the displacement via screw rotation. After each load increment, a scan was acquired while the sample was rotated (inside the testing device) around the laminographic axis (i.e., parallel to the specimen thickness direction). This axis was inclined with respect to the transmitted X-ray beam direction by an angle $\theta \approx 65$ °. A schematic view of the laminography setup together with the loading device is shown in Figure 1(a). The experiment was performed on beamline ID19 of the European Synchrotron Radiation Facility (ESRF), Grenoble, France. A total of 3,000 radiographs per turn were obtained with a 25 keV pink beam under continuous sample rotation with an indirect detector system [34] providing an effective voxel size of 0.65 µm. The series of acquired 2D projections is then used to reconstruct 3D volumes by using a filtered-back projection algorithm [35]. The parameter optimization has been performed automatically using a GPU-accelerated implementation of this algorithm [36, 37]. The scanned region was positioned in one of the two ligaments where shear occurred (Figure 1(b)). The exact dimensions of the notched sample are given in Ref. [8].

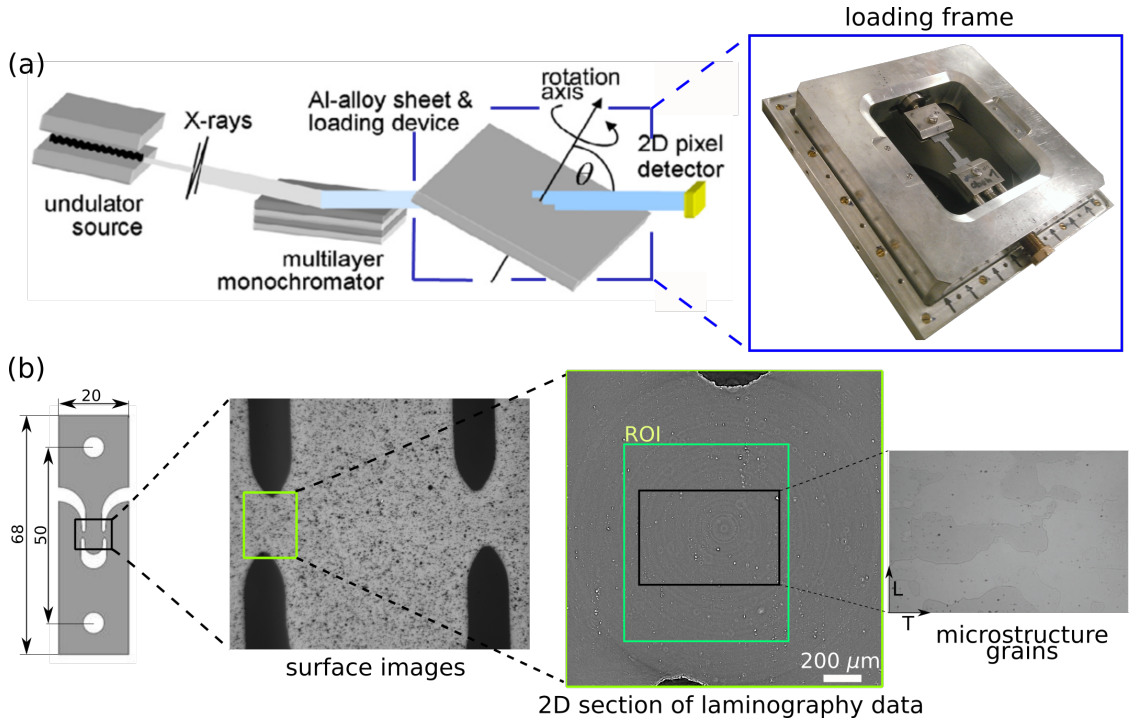

Figure 1: (a) Schematic view of the laminography setup. (b) Shear sample geometry and position of the scanned zone. In the section of the scanned region the representation of microstructural grains is shown [38]

2.2. Material

AA2198 was developed by Constellium. The alloy has a slightly lower copper content compared to AA2098 and also has some other minor chemistry adaptations (Ag, Zr ...) to optimize toughness. Table.1 gives the chemical composition limits for AA2198 alloy. In this work, recrystallized AA2198 aluminum-copper-lithium alloy sheets with a nominal thickness of 2 mm were supplied by Constellium. The alloy in T851 (artificially aged) heat treatment condition was studied. The alloy is obtained by cold rolling followed by industrial finishing treatment: solution heat treatment, water quench, stretch and artificial aging to obtain T851 temper. In the following, the rolling direction is noted as L, the long transverse direction as T and short transverse direction (thickness direction) as S. The yield strength was $\sim$ 440 MPa, and the ultimate tensile strength $\sim$ 500 MPa [23]. Therefore, the heat treatment endowed the material low work hardening. The intermetallic particle volume fraction was found to

be $\sim 0.3 - 0.4$ %, while the initial porosity was very low (i.e., < 0.03 vol%) [23]. The grain size was measured by a mean linear intercept method on EBSD data as 82 μm in L, 80 μm in T and 20 μm in S directions [23]. More details on the material properties can be found in Refs. [26, 23, 39]. The very low volume fraction of secondary phases makes this material very challenging for Digital Volume Correlation (DVC) since it relies on natural markers [25, 26].

	Cu	Li	Zn	Mn	Mg	Zr	Si	Ag	Fe
wt.%	2.9-3.5	0.8-1.1	$\leq$0.35	≤ 0.5	0.25-0.8	0.04-0.18	≤ 0.08	0.1-0.5	≤ 0.01

Table 1: Nominal chemical composition limits of 2198 alloy (wt %).

In the experiment reported herein, the loading was applied in the L-direction, and the S-direction corresponds to the thickness direction of the sample. Figure 1(b) illustrates the grain orientations and their relative size with respect to the scanned region.

2.3. Digital Volume Correlation

The reconstructed volume is represented by a discrete gray level field (8-bit deep) of the spatial (voxel) coordinate $\mathbf{x}$. It had a size of $2560 \times 2560 \times 2300$ voxels. The physical size (length) of one cubic voxel was equal to 0.65 μm. Each voxel inside the reconstructed volume contains the gray level information determined by the material ability to absorb X-rays. In the present case, image contrast was mainly due to heavy intermetallic particles of micrometer size. The part of the reconstructed volume that was used in DVC will be designated as the Region of Interest (ROI). The ROI position is depicted in Figure 1(b) while in the z direction the ROI and sample mid-thickness planes coincide. The original gray level volumes were coarsened (i.e., blocks of 8 voxels were replaced with the corresponding supervoxel having the mean gray level of the block) to be able to cover larger regions in DVC calculations. Therefore an ROI of size $640 \times 800 \times 688$ supervoxels was used for DVC analyses.

DVC used herein is an extension of 2D finite-element Digital Image Correlation [40, 41]. The principle of DVC consists in matching the gray levels f in the reference configuration $\boldsymbol{x}$ and those of the deformed volume g such that

$$f(\boldsymbol{x}) = g[\boldsymbol{x} + \boldsymbol{u}(\boldsymbol{x})] \tag{1}$$

where $\boldsymbol{u}$ is the displacement field with respect to the reference volume. In real applications the previous conservation of gray level is not satisfied, especially in laminography where deviations appear not just due to acquisition noise but also due to reconstruction artifacts because of missing information (angles) [42]. Consequently, the solution consists in minimizing the gray level residual $\rho(\boldsymbol{x}) = f(\boldsymbol{x}) - g[\boldsymbol{x} + \boldsymbol{u}(\boldsymbol{x})]$ by considering its L2-norm with respect to kinematic unknowns associated with the parameterization of the displacement field. Since a global approach was used in this work, the whole ROI was considered, and the global residual Φ_c

$$\Phi_c^2 = \sum_{ROI} \rho^2(\boldsymbol{x}) \tag{2}$$

was minimized with respect to the unknown degrees of freedom u_p when the displacement field is written as

$$\boldsymbol{u}(\boldsymbol{x}) = \sum_p u_p \boldsymbol{\Psi}_p(\boldsymbol{x}) \tag{3}$$

where $\boldsymbol{\Psi}_p(\boldsymbol{x})$ are the chosen displacement fields for the parameterization of $\boldsymbol{u}(\boldsymbol{x})$. Among a whole range of available fields, finite element shape functions are particularly attractive because of the link they provide between the measured displacement fields and numerical models. Thus, a weak formulation based on C8 finite elements with trilinear shape functions was chosen [43].

2.3.1. Strain characterization

From the mean deformation gradient tensor over each C8 element, the Hencky (logarithmic) strain tensor and subsequently its second invariant will be used in the sequel, the von

Mises equivalent strain being

$$\Delta\epsilon_{eq} = \sqrt{\frac{2}{3}\Delta\boldsymbol{\epsilon}_d : \Delta\boldsymbol{\epsilon}_d} \tag{4}$$

where $\Delta\boldsymbol{\epsilon}_d$ denotes the deviator of the logarithmic incremental strain tensor $\Delta\boldsymbol{\epsilon}$. Further, the Lode parameter [4] associated with strain increments ($\mu_{\Delta\epsilon}$) is defined as

$$\mu_{\Delta\epsilon} = \frac{2\Delta\epsilon_{II} - \Delta\epsilon_I - \Delta\epsilon_{III}}{\Delta\epsilon_I - \Delta\epsilon_{III}} \tag{5}$$

where $\Delta\epsilon_i$ ($i = I, II, III$) represent eigen strains ($\Delta\epsilon_I \geqslant \Delta\epsilon_{II} \geqslant \Delta\epsilon_{III}$).

The DVC uncertainty was evaluated by correlating two scans of the unloaded sample with (denoted "rbm") and without (denoted "bis") a small rigid motion applied between subsequent acquisitions. Due to noise contribution and reconstruction artifacts, these two volumes were not identical. Therefore, the measured displacement field accounted for cumulated effects of laminography and DVC on the measurement uncertainty [25]. The uncertainties were evaluated by the standard deviation of the measured strain fields. Figure 2(a) shows the standard equivalent strain uncertainty levels for different element sizes ℓ expressed in supervoxels. Decreasing the element size is followed by an increase of the strain uncertainty. The element size used in this work was $\ell = 16$ supervoxels (length) for all three directions, which yielded a standard equivalent strain uncertainty of 0.51 %. These levels represent the limit below which the estimated strains are not trustworthy. Minimal effect is observed for the two different analyses (with or with no rigid body motions). Figures 2(b-d) display the eigen strain uncertainties. For the selected element size $\ell = 16$ supervoxels, the uncertainty levels for ϵ_k ($k = I, II, III$) were 0.79 %, 0.36 % and 0.43 %, respectively.

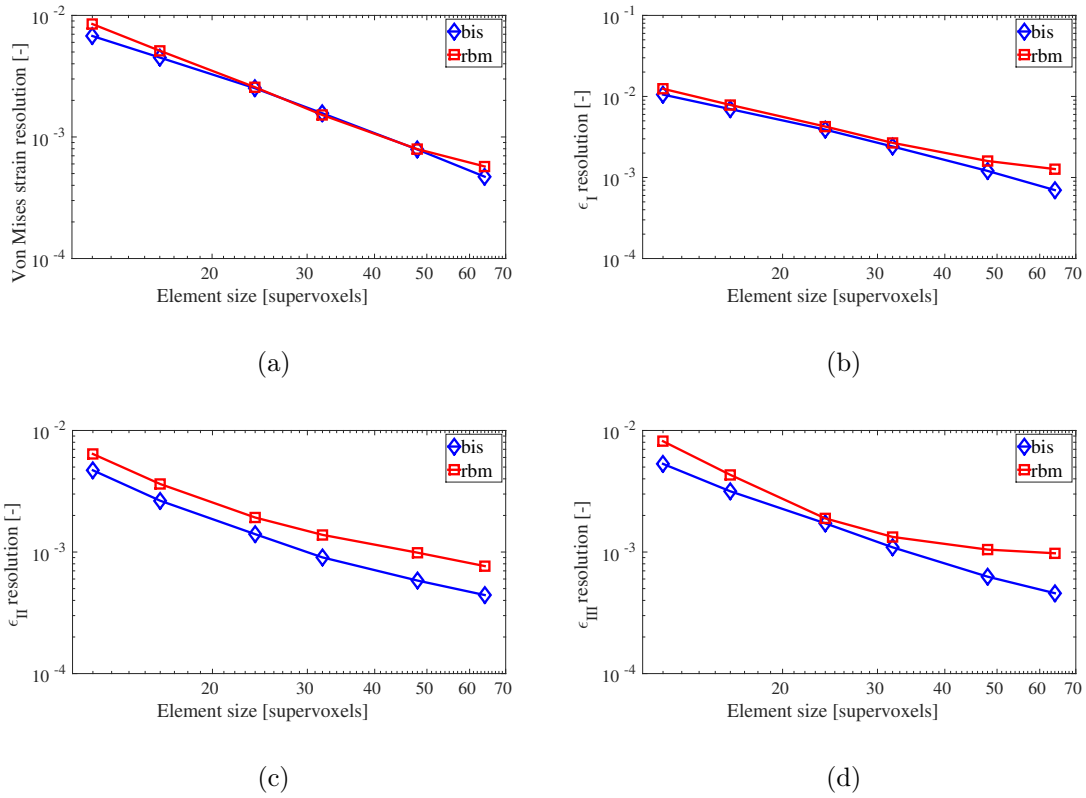

Figure 2: Standard strain uncertainties as functions of the element size for the equivalent strain (a), ϵ_I (b), ϵ_{II} (c), and ϵ_{III} eigen strains

2.3.2. DVC calculations

Direct DVC results refer to the solutions obtained by correlating the undeformed volume (state (0)) and one of the deformed configurations (state (n)), while incremental calculations stand for the correlation between any deformed volume (state (n)) and subsequent (state $(n+1)$) configuration. Due to large strains in this work, incremental DVC calculations will be reported. Since the global coordinate system was identical for all incremental calculations, the displacement fields can be superimposed [44]. This is carried out by interpolating incremental results (n)-$(n+1)$ on the deformed mesh from the loading step (0)-(n). This operation resulted in a part of the boundary nodes from the initial DVC ROI without kinematic information since ROIs in incremental calculations kept a constant size. By con-

ducting such analyses, one obtains DVC registrations from the undeformed configuration to the very end of the loading history. This operation is the basic principle of a *cumulative* procedure in post-processing the DVC results and will be used in the sequel. Thus, there are two different ways of displaying incremental results. First the fields are shown on the reference configuration of each incremental DVC analysis. Second, all results are expressed in a Lagrangian way by reprojecting all measured incremental fields as difference between *cumulated* calculations.

2.3.3. 3D image analysis

To segment damage, a region growing algorithm [45] was used. It was chosen to project damage onto one surface to obtain a surface void fraction rather than a void volume fraction, as will be discussed later on. The surface onto which the damage was projected was the future fractured surface (projection approximately along T direction over a length of 144 μm). The surface void fraction was computed as the number of pixels that belonged to the segmented projected damage divided by the number of pixels of the total area.

3. Results

3.1. DVC fields

Beside the scans in the undeformed configuration, 8 additional acquisitions were conducted during the experiment, the last one being the scan of the fractured ligament. The load levels associated with the machine displacement are shown in Figure 3. Each symbol denotes the position at which a new scan was performed. The tests showed very good repeatability in terms of stresses, machine displacement and strain to fracture despite the small ligament. The reader is referred to [39] for the repeatability of such kind of test and this material.

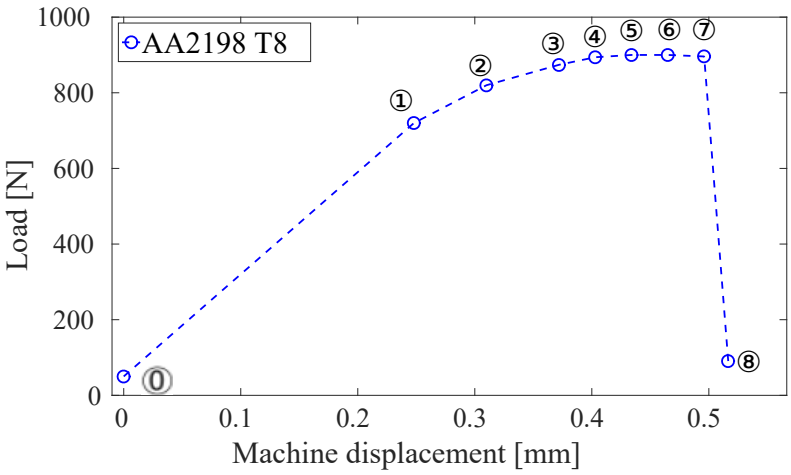

Figure 3: Load levels vs. machine displacement. Each symbol depicts a scan acquisition

The DVC calculations were challenging since highly localized deformation occurred in the shear plane. Thus, instead of starting with no initialization, the registrations were initialized with *a priori* chosen displacement fields (Figure 4). The initialization fields were obtained by first conducting two independent DVC analyses on two sub-ROIs that were positioned out of the shear plane and mostly experienced rigid body motions. The initial guess for the displacement field in the remainder of the ROI was linearly interpolated between the values obtained for the two sub-ROIs. The resulting field served as an initial guess (see displacement profiles in Figure 4) for the corresponding DVC calculations.

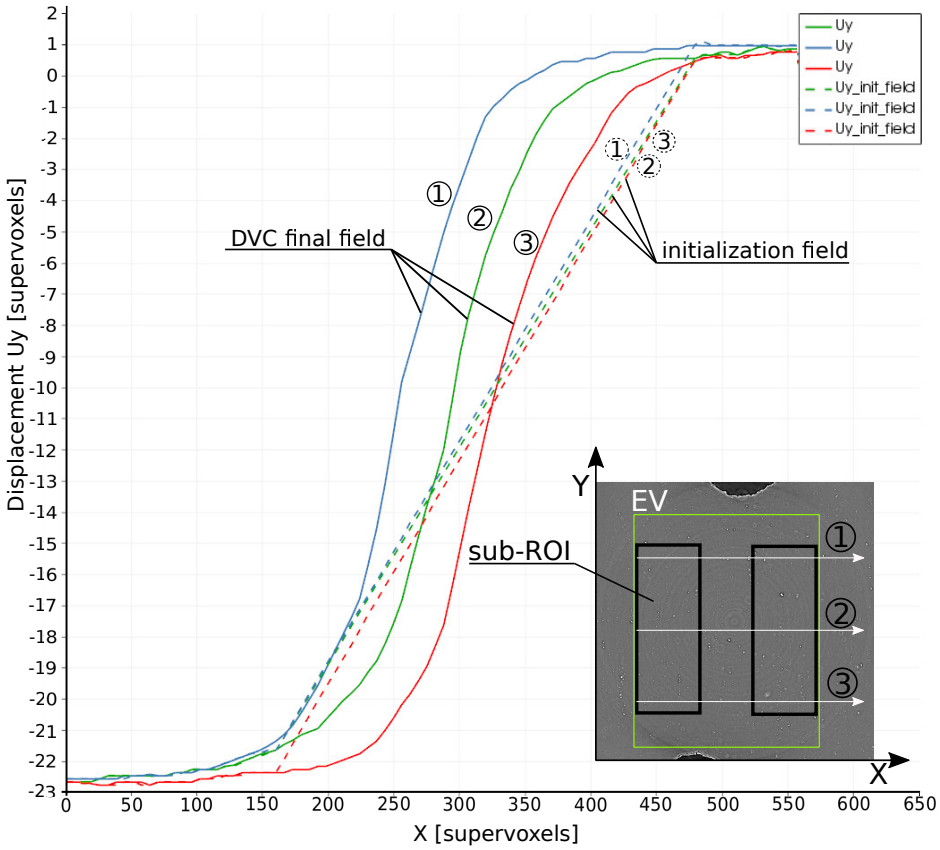

Figure 4: Displacement profiles from initialization (dashed lines) and final (solid lines) DVC results for one loading step

The gray level DVC residuals are shown in Figure 5. The fact that ring artifacts are observed in the residual maps revealed the successful registration where initial differences between the gray level volumes decreased to noise level and artifacts (i.e., rings for this case). Had the artifacts disappeared, it would have meant that the registration had tracked the rings and not material motions. In the remainder of the ROI, spots with slightly higher residuals were located in the shear plane. The fact that there existed zones in which the brightness was not not conserved had their mechanical interpretation and will be detailed in the sequel.

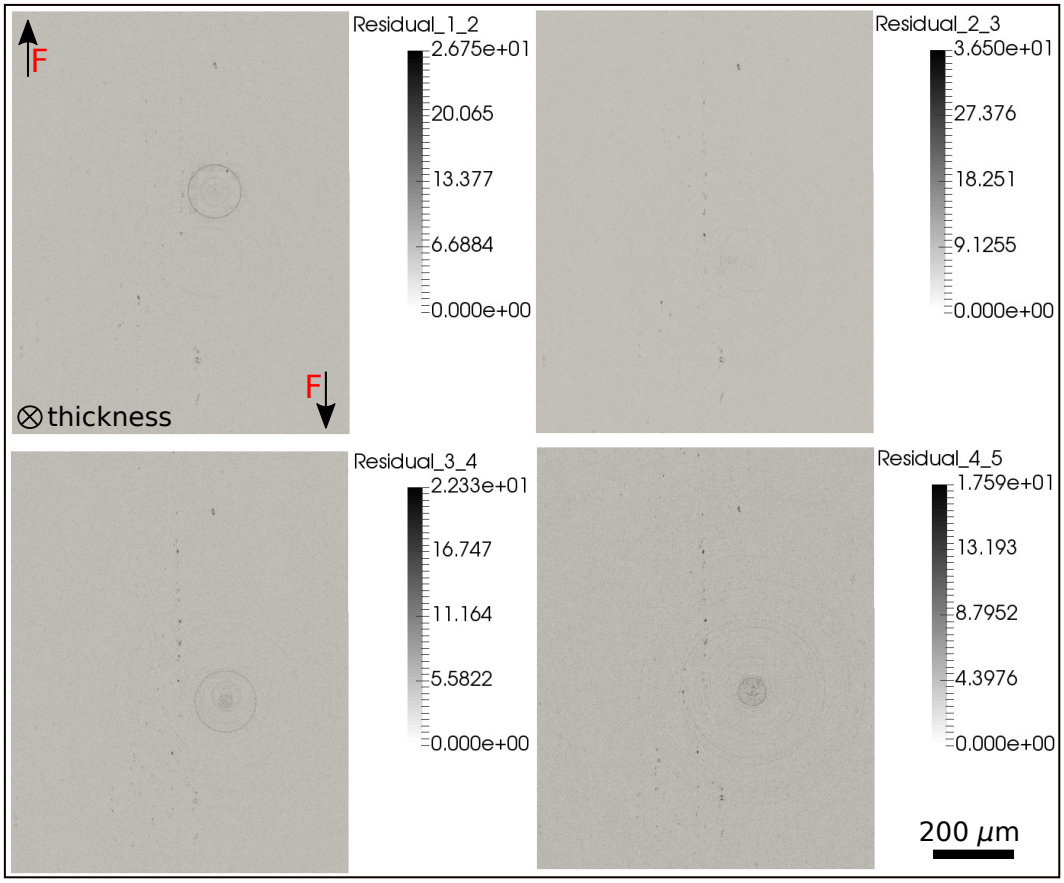

Figure 5: Gray level residual maps plotted for the mid-thickness section of the ROI for different loading steps (noted in color bar title)

Figure 6 shows von Mises incremental strain maps plotted on mid-thickness sections of the ROI. During the first load step (0)-(1) (field not shown in Figure 6), the specimen was mainly in the elastic regime and the resulting strain levels were close to the estimated uncertainties. From the second incremental loading step on, the strain field were localized in one shear band. The strain levels in the band were $> 5\%$, namely, one order of magnitude higher than the reported measurement uncertainty (Figure 2(a)), which indicates a clear mechanical signal.

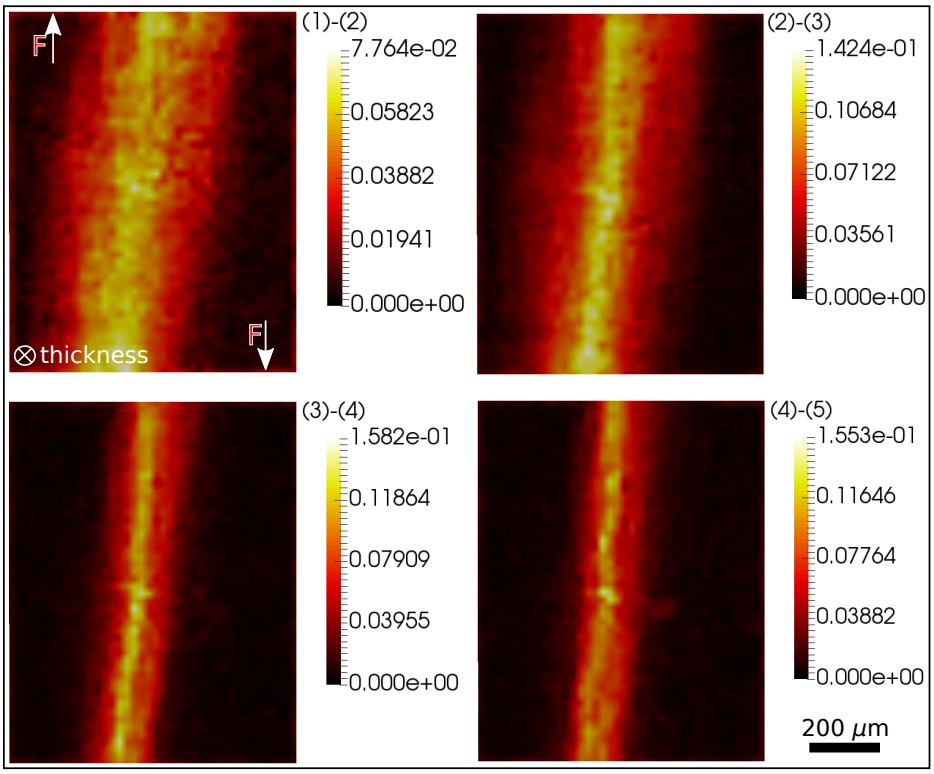

Figure 6: Von Mises incremental strain maps from DVC calculations plotted for the ROI mid-thickness section (L-T plane)

In the following loading steps, the strain field localized even more into a thinner band. This observation corresponds to a localized situation where all macroscopically added energy to the system through force and displacement was dissipated in a thin strained band. Interestingly, the highly strained band (loading step (4)-(5)) was not perfectly straight, but showed some curvatures. This effect could be induced by the underlying grains and grain boundary positions.

In Figure 7, von Mises incremental strain profiles along line ξ are reported for different loading steps. Since incremental results are reported in a Lagrangean way (see Section 2.3.2), the strain peak position remained essentially motionless in the graph. The strong localization into a thinner band for the last loading steps is clearly observed.

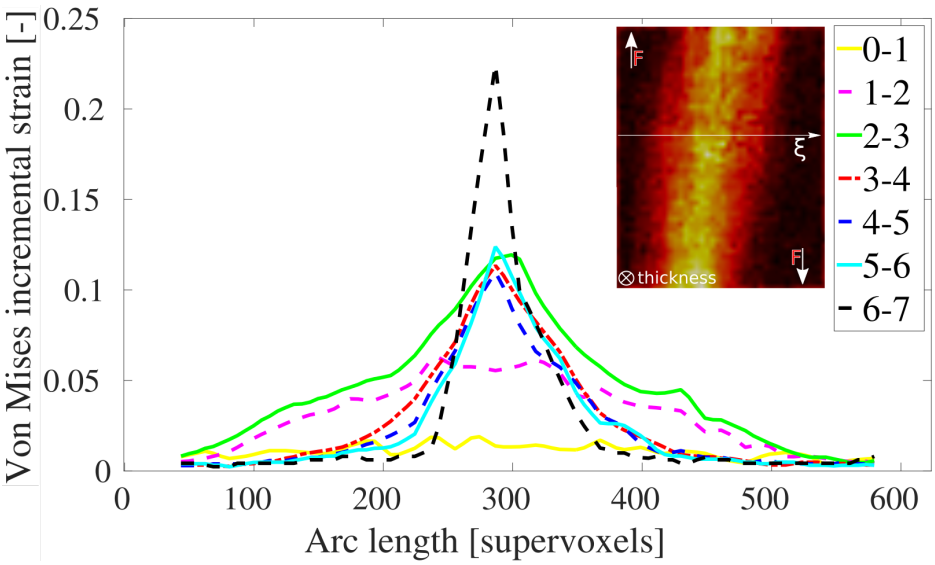

Figure 7: Von Mises incremental strain profiles from DVC calculations. The position of the profile axis ξ is denoted on the strain map inset

The *cumulative* operation (see Section 2.3.2) yielded von Mises strain fields between undeformed configuration (0) and subsequent stages (n) as shown in Figure 8. Due to this procedure, part of the boundary nodes from the initial DVC ROI remained without any kinematic information as illustrated in the figure. Unlike incremental plastic activity, in these strain maps the band remained significantly wider due to cumulated plasticity from the early loading steps on.

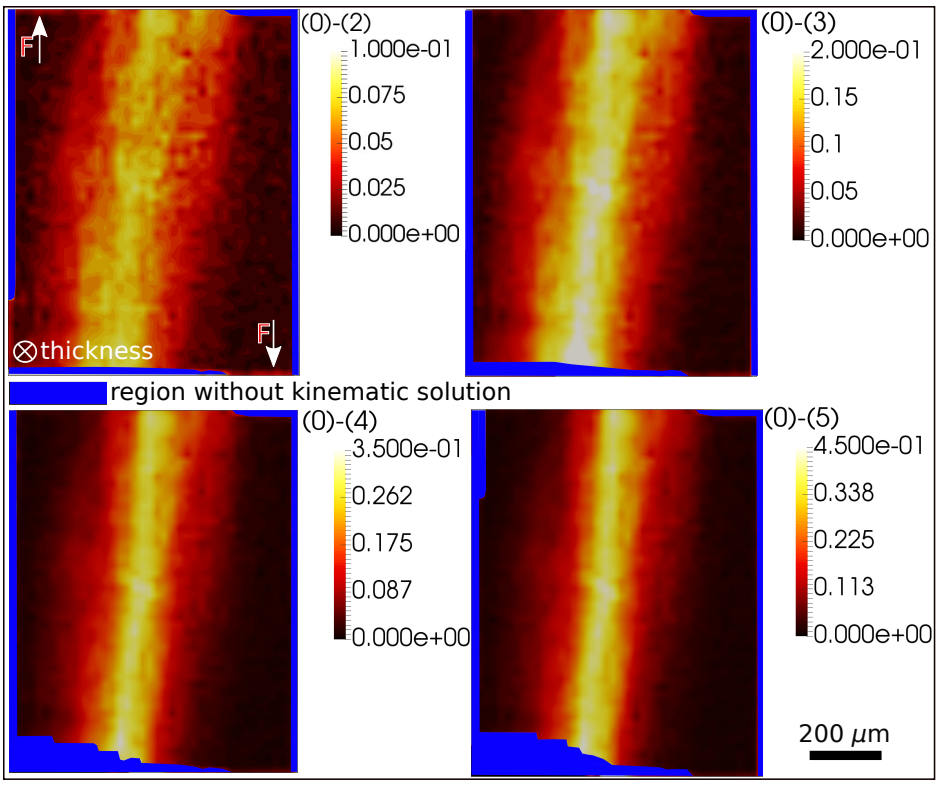

Figure 8: Von Mises strain maps from *cumulated* incremental DVC calculations plotted for the ROI mid-thickness section (L-T plane)

In Figure 9, von Mises strain profiles along line ζ from *cumulated* incremental DVC calculations are reported for different loading steps. The results are expressed in Lagrangian way and the band position did not move for all loading steps. The strain level inside the band for the last reported loading step was $\epsilon_f \approx 0.65$.

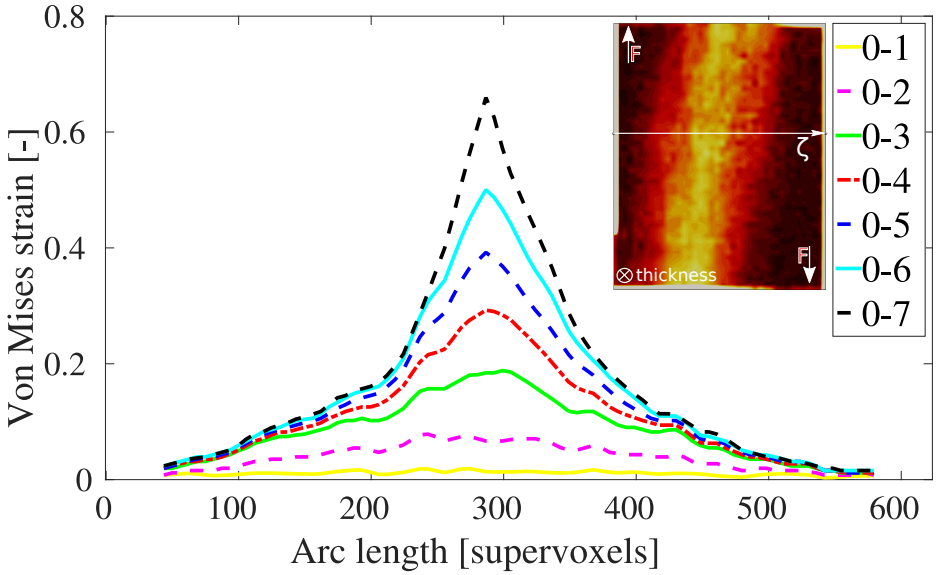

Figure 9: Von Mises strain profiles from *cumulated* incremental DVC calculations. The position of the profile axis $\zeta$is denoted on the strain map illustration

Figure 10 shows Lode parameter maps for incremental strains $\mu_{\Delta\epsilon}$ plotted for the ROI mid-thickness section. From the second loading step on, the position of the band can be distinguished from the remainder of the ROI. The values in the band were close to zero. However, in the remainder of domain with DVC elements with low strains (close to uncertainty levels) the Lode parameter could not be assessed in a trustworthy way. It was important to recognize this difference and separate these two types of data.

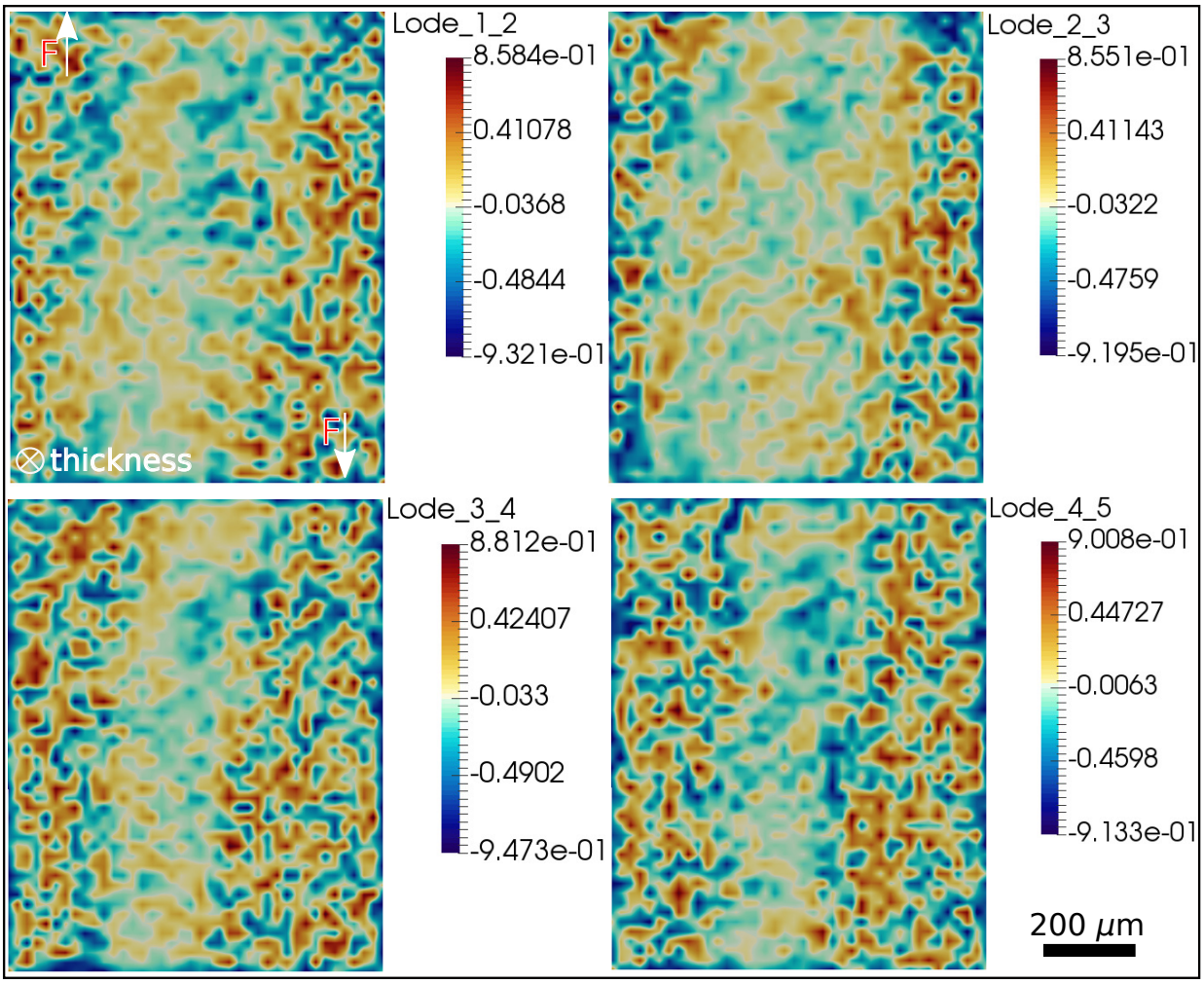

Figure 10: Lode strain parameter $\mu_{\Delta\epsilon}$ maps from incremental DVC calculations plotted for the ROI mid-thickness section

This effect is illustrated in Figure 11. The graph contains von Mises incremental strains $\Delta\epsilon_{eq}$ and Lode parameter $\mu_{\Delta\epsilon}$ for mechanical (loading step (3)-(4)) and noisy situations ("bis" case from the uncertainty analysis). In the region out of the band, the Lode parameter displayed similar oscillations. In the shear band, the Lode parameter was stabilized, thereby indicating higher mechanical signal, with values close to zero accompanied by very high strain increments.

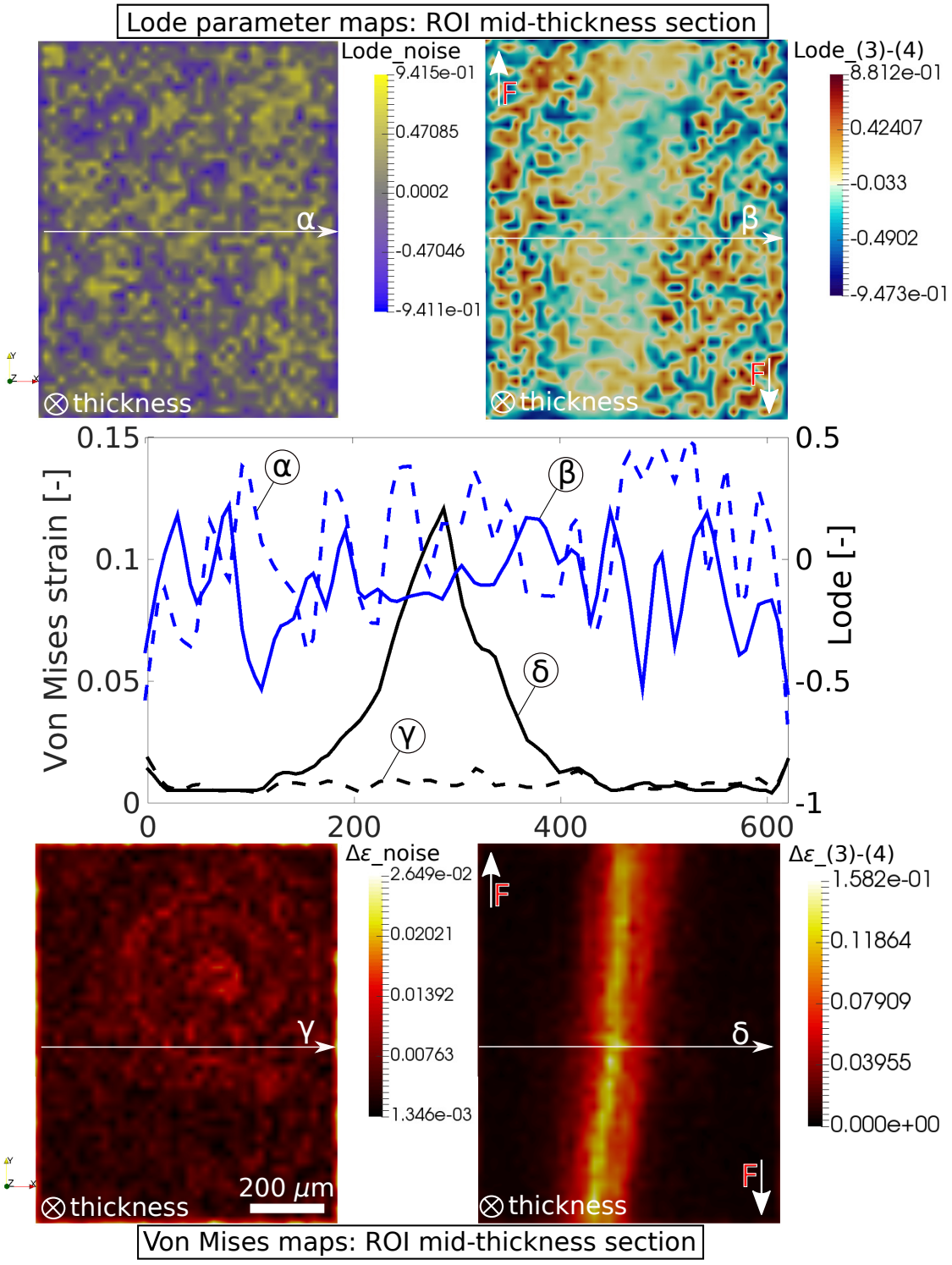

Figure 11: Von Mises incremental strain $\Delta\epsilon_{eq}$ and Lode parameter $\mu_{\Delta\epsilon}$ for mechanical (loading step (3)-(4)) and noisy data ("bis" case from the uncertainty analysis)

According to Equation (5), the uncertainty for the numerator of Lode parameter $\mu_{\Delta\epsilon}$ is estimated as

$$\Sigma_\mu = \sqrt{{\Sigma_I}^2 + 4{\Sigma_{II}}^2 + {\Sigma_{III}}^2} \tag{6}$$

where Σ_j $(j = I, II, III)$ denotes standard uncertainty of the (incremental) eigen strains. Error bars associated with the Lode incremental strain measurements are then obtained as

$$e(\boldsymbol{x}) = \frac{\Sigma_\mu}{\sqrt{3}\Delta\epsilon_{eq}(\boldsymbol{x})} \tag{7}$$

In this equation, it is assumed that the denominator is significantly higher in level than the numerator of the Lode parameter (i.e., in shear, $\mu_{\Delta\epsilon} \to 0$). Further, the eigen strain difference $\Delta\epsilon_I - \Delta\epsilon_{III}$ is assumed to be close to $\sqrt{3}\Delta\epsilon_{eq}$ (this expression is exact in pure shear).

The Lode parameter $\mu_{\Delta\epsilon}$ profiles with the corresponding error bars are shown in Figure 12. The values were taken from the profile reported in Figure 7 for loading step (3)-(4). There is a significant error decrease in the strained band with a clear mechanical signal.

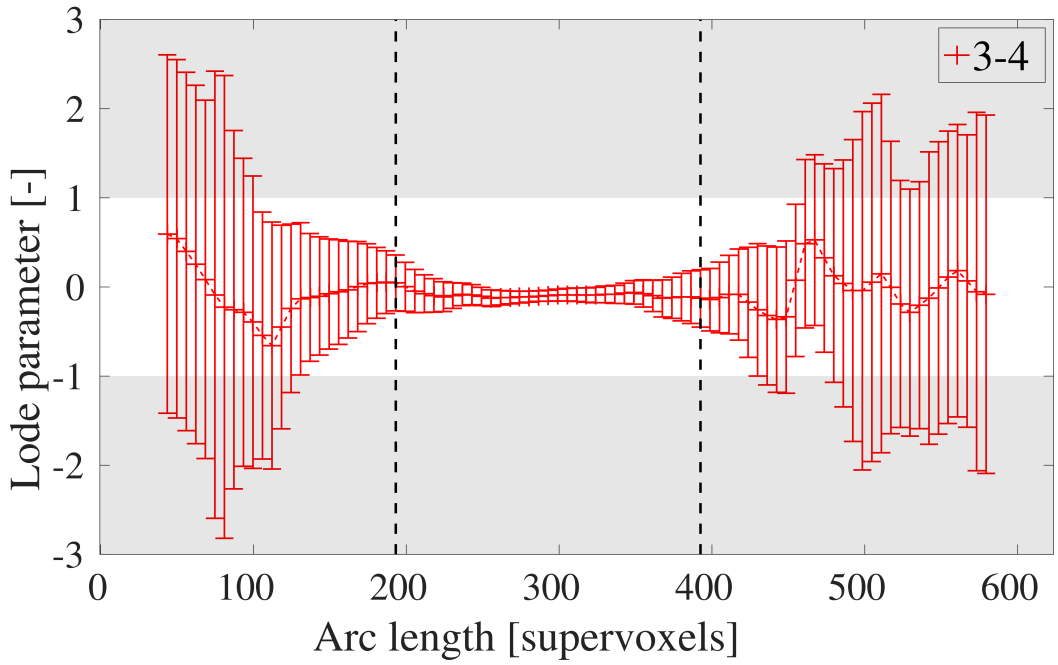

Figure 12: Lode parameter $\mu_{\Delta\epsilon}$ profile (from Figure 13(a)) for loading step (3)-(4)) with the corresponding error bars. The area between dashed lines corresponds to the strained band position (i.e., $\Delta\epsilon_{eq} > 2$ %). The values of Lode parameter inside shaded areas are theoretically non-admissible

In this context, it was possible to plot Lode parameter $\mu_{\Delta\epsilon}$ profiles with the distinction made between mechanical and noisy signals. This distinction was obtained by reporting only the Lode parameters for the DVC elements where von Mises incremental strain levels satisfy the condition $\Delta\epsilon_{eq} > 2$ % (Figure 13(a)). The value 2% was chosen as certain offset (i.e., factor 4) with respect to the reported strain uncertainty (0.5%). It is worth noting that the Lode parameter $\mu_{\Delta\epsilon}$ oscillates about a mean value close to zero. The level of oscillations was within the window determined by the measurement error shown in Figure 13(b) for the loading step (3)-(4).

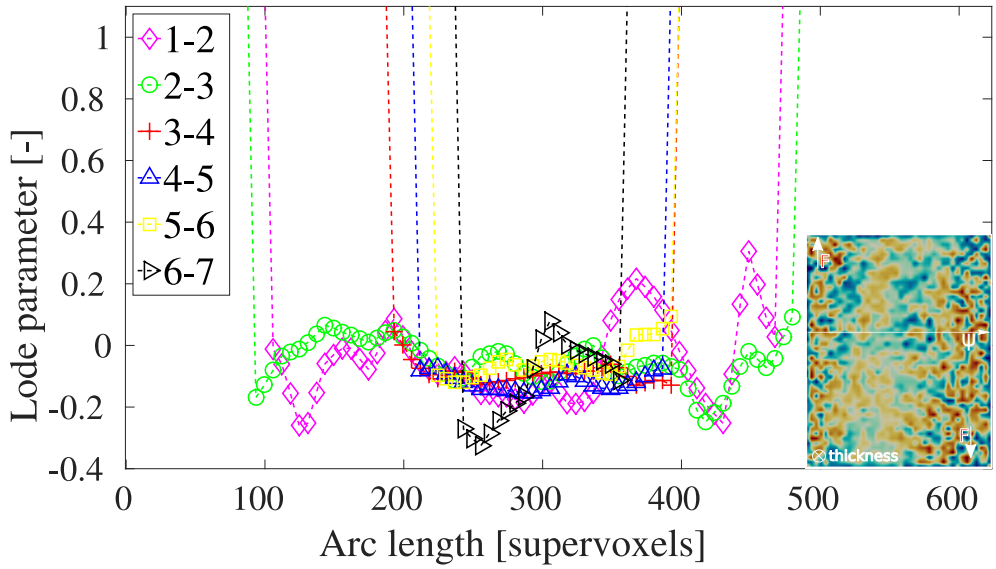

(a)

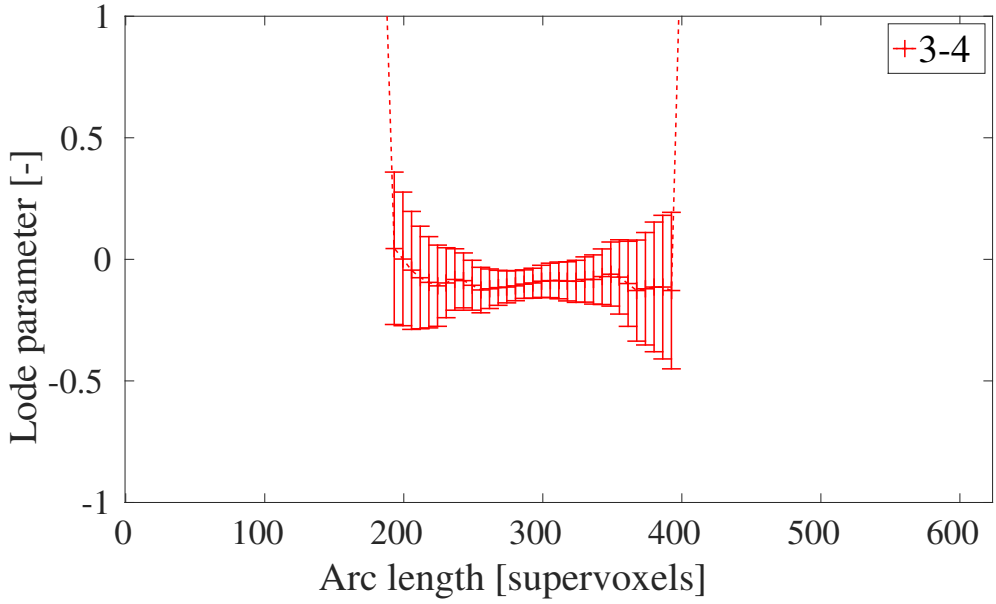

(b)

Figure 13: (a) Lode incremental strain parameter $\mu_{\Delta\epsilon}$ profiles from incremental DVC calculations. The position of the profile axis is denoted on the Lode map shown in the inset. (b) Trustworthy part of the Lode parameter $\mu_{\Delta\epsilon}$ profile in the shear band for loading step (3)-(4)) with the corresponding error bars

This result confirms the ability of DVC to measure Lode parameter $\mu_{\Delta\epsilon}$ for incremental strain fields. Let us recall that the stress Lode parameter is proportional to strain rate Lode parameter [4]. Hence, in the case of pure shear, zero is also a value expected for incremental strain Lode $\mu_{\Delta\epsilon}$ measurements as reported in the work.

In the literature [46], the strain rate Lode parameter is often reported for incompressible solutions

$$\mu = \frac{3\Delta\epsilon_{II}}{\Delta\epsilon_I - \Delta\epsilon_{III}} \tag{8}$$

The purpose of Figure 14 is to inspect possible differences between the two definitions of Lode parameter. The Lode parameters $\mu_{\Delta\epsilon}$ for four steps obtained from Figure 13(a) are compared with the assumption of incompressibility. The values for the loading steps (3)-(4), (4)-(5) and (5)-(6) do not differ significantly since there was no significant damage growth at this point. However, for the last reported DVC result (loading step (6)-(7)), the difference was more pronounced, which indicates the existence of volume variations (i.e., incompressiblity is no longer satisfied when damage grows even in shear).

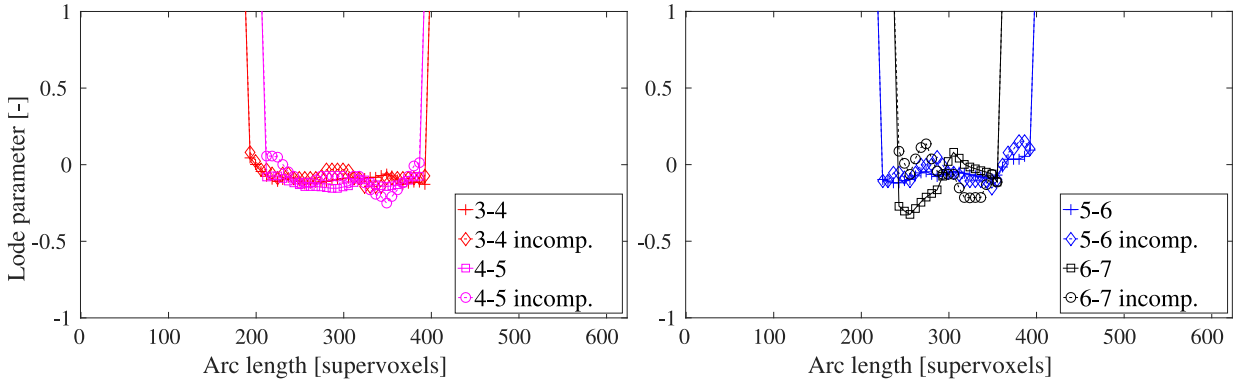

Figure 14: Trustworthy part of the Lode parameter $\mu_{\Delta\epsilon}$ profiles in the shear band for loading steps (3)-(4) and (4)-(5) (left) as well as (5-(6) and (6)-(7) (right) with and without the assumption of incompressibility

3.2. Damage activity

3.2.1. 3D renderings

The laminography data obtained with high resolution (1 voxel $\sim$ 0.65 μm) enabled us to follow the damage activity in a simple shear stress state. In Figure 15, 3D renderings of reconstructed volumes of the first four loading steps are shown where the Al-matrix was made transparent and only damage (dark gray levels) was seen. For load step (1), the machined notches are apparent in the rendering. The initial void volume fraction was extremely low for this alloy. Only for step (3) a comparatatively large damage feature nucleated. The damage feature is encircled in red in the figure. The equivalent strain within the band was already about 0.2 as measured by DVC.

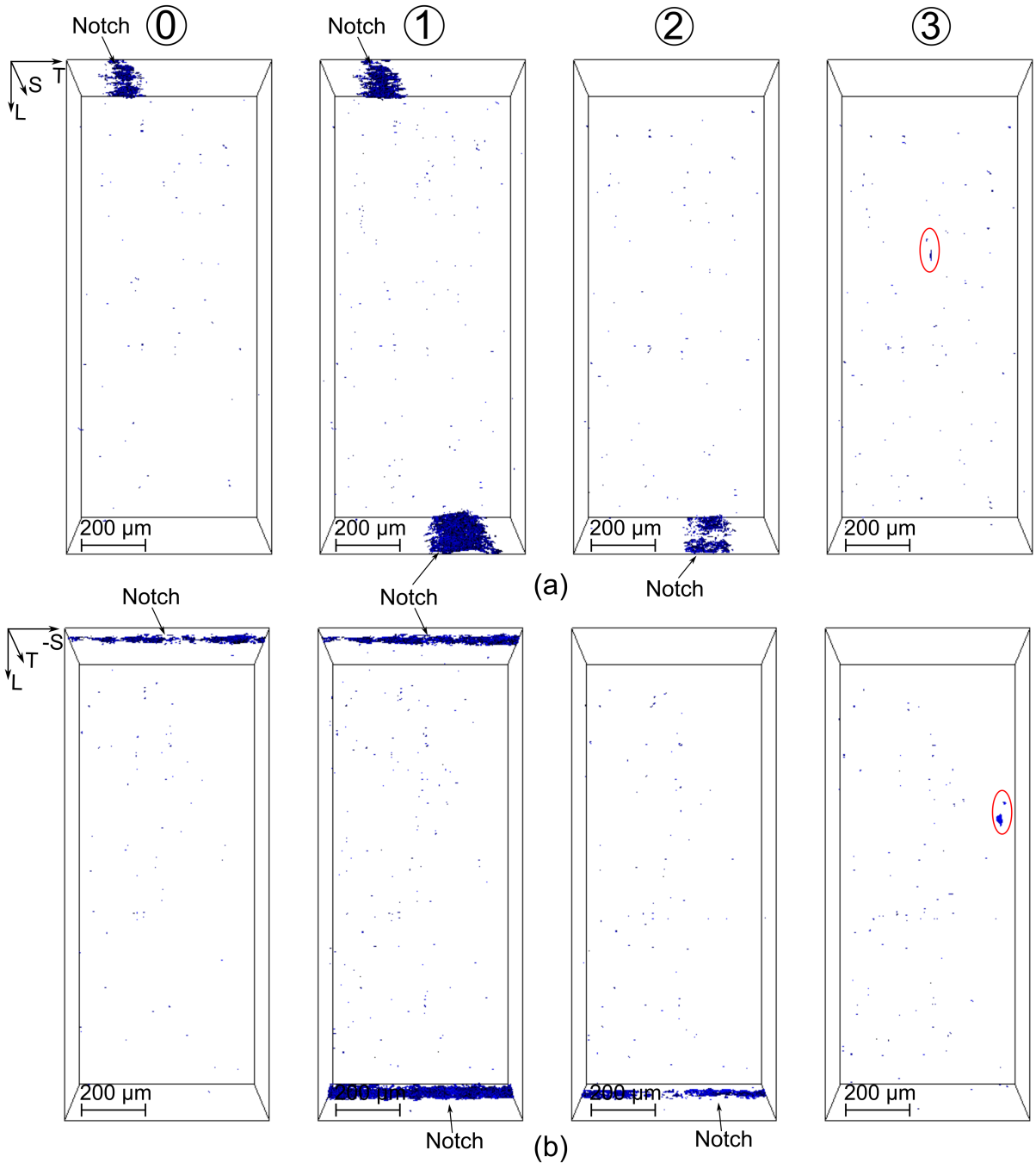

Figure 15: 3D damage renderings of the first four loading steps (0-3), (a) normal to the sheet plane (T-L), and (b) in the S-L plane

Figure 16 shows damage nucleation and growth during the last four load steps. It is

observed that the damage feature that nucleated in step (3) grew on in step (4). Damage also nucleated in other regions in the shear band. The length and width of the damage features corresponds to the grain shape of the material. Other flat cracks became visible in step (5). At step (7), the damage feature that nucleated first coalesced with other damage sites (see Figure 16(b) in the through-thickness view). This result shows the detrimental nature of these cracks that nucleate in shear, lead to an interaction between each other and ultimately in a reduction of the load carrying capacity. It is also seen that damage nucleated, grew and coalesced away from the notches, thereby confirming the appropriate design of the sample geometry to study deformation and damage in simple shear. For a FB600 steel cracks started clearly from the notches as the sample was not optimized for the material behavior [47].

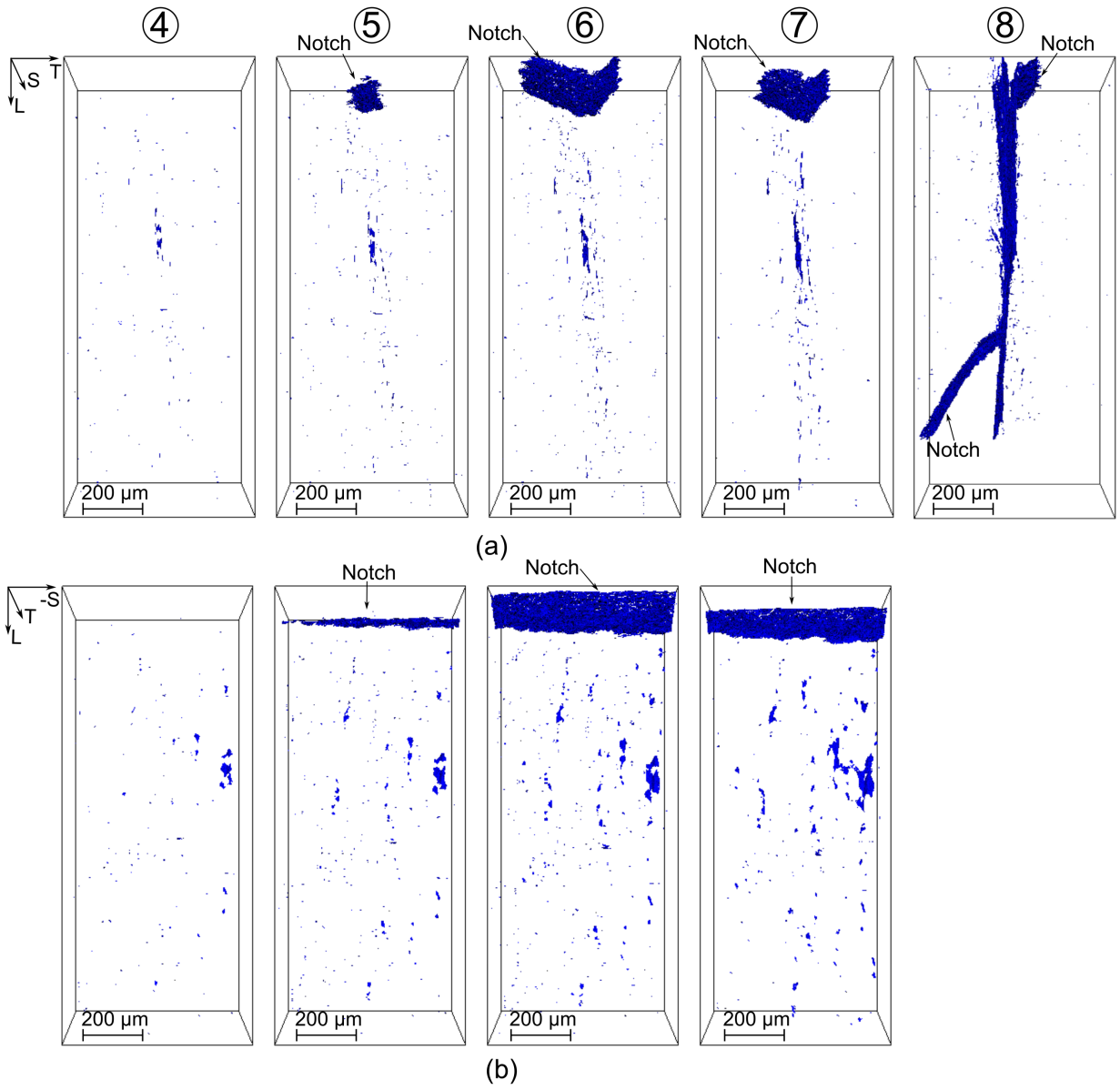

Figure 16: 3D damage rendering of the last four load steps (4-7), (a) normal to the sheet plane (T-L), and (b) in the S-L plane

3.2.2. Damage quantification

Figure 17 shows the raw volume data that were imaged by X-ray synchrotron micro-laminography. In order to focus on the shear band region where damage developed, a subvolume was selected with $200 \times 1,500 \times 1,000$ voxels. The damage features were projected

along the X axis (i.e., approx. T direction) onto the future fracture surface and the area was segmented into a binary image. Damage was quantified on the surface as surface void fraction because detrimental flat cracks has a very low volume fraction.

Damage growth was quantified as surface void fraction versus maximum equivalent strain from the DVC profiles (Figure 17(e)). Initially, the surface void fraction was less than 0.1%. It started to rise linearly with the equivalent strain from step (3) until fracture (up to 3%). Meanwhile, the maximum equivalent strain from the T profile reached more than 0.6. At a strain of 0.2, there is a change in damage growth rate. Up to a strain of 0.2 the activity was very limited. The increase in damage growth coincided with strain localization in the shear band (Figure 7). It is also observed that damage grew more slowly in shear than for a 'shear to tension' loading path change [23].

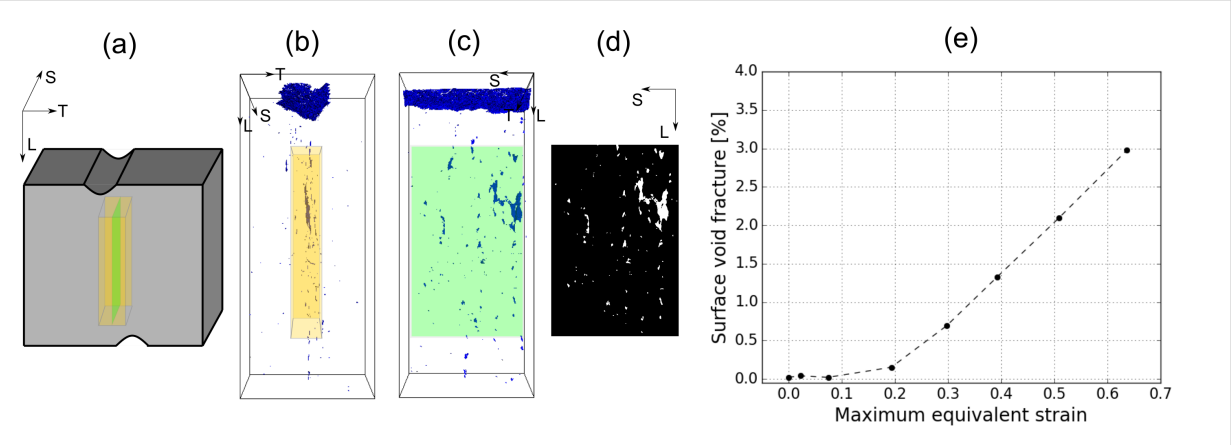

Figure 17: Damage quantification. (a) Schematic illustration of the complete scan. (b) Indication of the ROI in the scan in the L-T (b) and L-S (c) planes. (d) result of the projection and binarization. (e) surface void fraction in the ROI as a function of maximum equivalent strain measured by DVC

3.2.3. Damage micromechanisms

Figure 18 shows in more detail the nucleation and growth of different damage features found in the shear zone in 2D sections. In particular, the nucleation and growth of an elongated feature is shown in Figure 18(a) with its significant size (along both loading and

thickness directions). It seems to be an important factor that influenced the final failure, as it lied on the final fractured surface. The flat crack continuously propagated from loading step (4) on and it coalesced into a long flat crack up to 135 μm at the final step (7) before fracture. No intermetallic particle is attached to this damage feature. It could nucleate on grain boundaries or also within grains [45], given the size and width of the damage feature. Remarkably, this shear-induced feature has never been observed before in the same sample geometry for other alloys (i.e., FB600 steel [22], AA2024T3 [6]). Due to the limited resolution, features below the micrometre scale could not be clearly observed to identify the nucleation mechanism and a higher magnification would be needed.

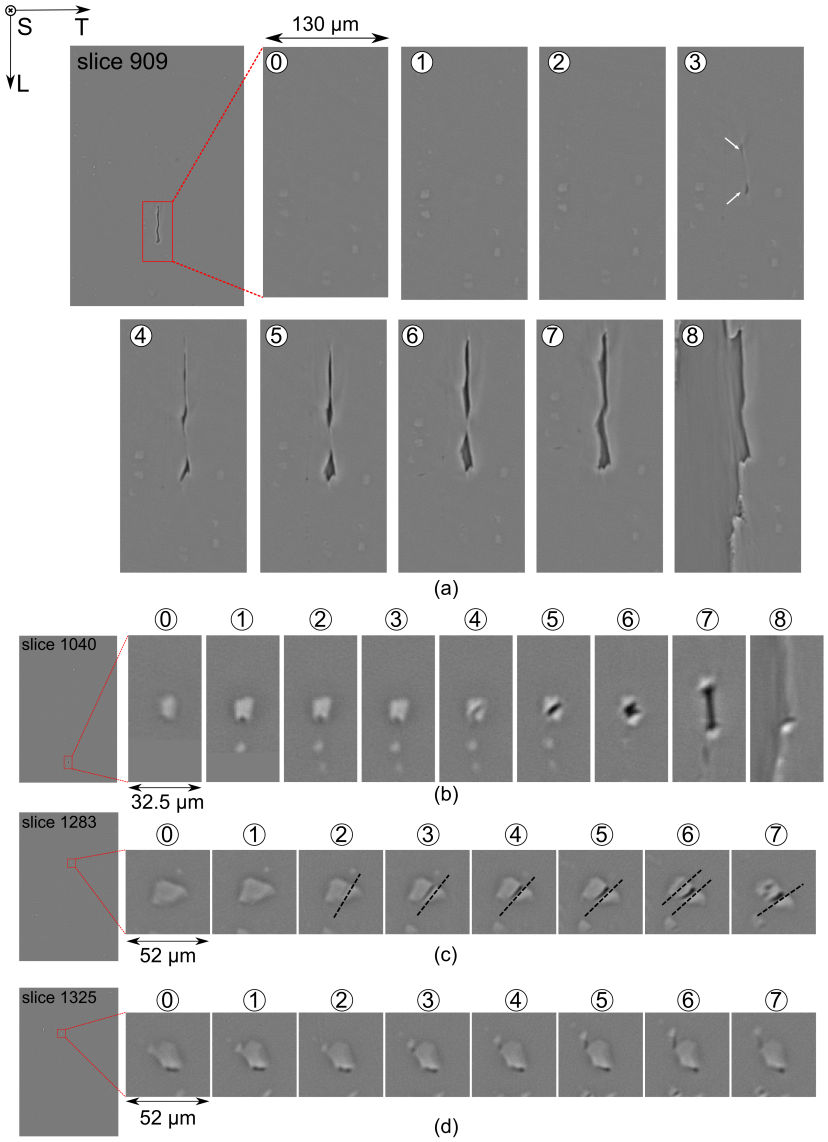

Figure 18: 2D sections of reconstructed laminography data showing damage features found in the shear zone. (a) Nucleation and growth of elongated damage feature along the shear plane. (b) Damage nucleation and growth from an intermetallic particle. (c) Intermetallic particle cracking. d) Initiation of a crack between two particles

Another damage feature is particle cracking. Three particles with a length of few tens of µm were found and traced in Figure 18(b-d). The particles rotated under shear loading until they broke into several pieces. The evolution of the particle on the plane 2 µm from the

mid-section is shown in Figure 18(b). It starts to debond from the matrix at step (1) and breaks at step (4). The particle crack is oriented at bout 45° with respect to the macroscopic loading direction, which is normal to the principal stress [6, 48]. The particle breaks into two pieces and an elongated void was generated at step (7). It was also one of the main detrimental features eventually contributing to the macrocrack. It should be noted that void growth was observed to take place in shear (i.e., stress triaxiality close to zero) due to the fact that rigid particle debris kept the void open.

Two more particle related cracks are shown in Figure 18(c,d). The particle (160 μm away from the mid-section, Figure 18(c)) with a length of about 20 μm broke at step (2) with a crack orientation of 56°. However, more cracks appeared locally and the angle decreased to 38°. The particle observed in the plane about 288 μm from the mid-plane (Figure 18(d)), with a diameter of about 15 μm had a tiny void less than 5 μm in length attached at the bottom. A small part split away from the large particle resulting in a crack between the main particle and the debris.

4. Conclusion

In the present work, a region of interest in a flat specimen where local stress states were close to simple shear was imaged in 3D by synchrotron laminography under *in situ* mechanical loading. Digital volume correlation (DVC) was used to determine the strain fields inside the loaded material. The main conclusions were:

- The ability of DVC in its global formulation to perform measurements in challenging conditions with high strain levels localized in a shear band was demonstrated. The correlation was possible thanks to sufficient natural contrast features (i.e., due to highly attenuating intermetallic particles embedded in Al matrix, see Figure 1). The sparsity of natural contrast made the present situation even more challenging. However, by

means of initialization fields, successful DVC registrations were obtained, which was confirmed by the residual maps (Figure 5).

- The (equivalent Hencky) strain to failure in the bulk of the material was measured (i.e., $\epsilon_f \approx 0.65$).

- Incremental strain Lode parameter $\mu_{\Delta\epsilon}$ fields as post-processed from incremental DVC displacements proved to be sensitive enough to confirm generalized shear stress states (i.e., values close to zero were found in the shear band). The stress Lode parameter being proportional to the strain rate Lode parameter indicates zero as target value for incremental strain Lode measurements, as reported in this work. This finding can be used in other cases (e.g., Compact Tension mode-I opening).

- Damage nucleating from the fourth loading step on was identified in the scanned ligament, mostly concentrated within the shear plane away from free surfaces. The observation that damage nucleated away from the notches is one of the most important finding, and an additional proof of proper design for the shear sample geometry used herein [8].

- Damage was quantified as the void surface fraction and a function of equivalent strain. Damage grew more quickly beyond 0.2 of equivalent strain.

- The first type of damage features has mainly elongated shapes and accumulated in the bulk of the ligament. Their sizes suggested that they were grain-related and detrimental due to their size.

- The second type of damage features corresponding to intermetallic particle breakage normal to the maximum principal stress direction was also detected but with minor influence on the final failure of the ligament. Void growth was seen to take place during shear as rigid particle debris kept the voids open.

Acknowledgements

The financial support of Agence Nationale de la Recherche (ANR-14-CE07-0034-02 grant for COMINSIDE project and LAMBDA ANR-17-CE08-0051) is gratefully acknowledged. The authors also acknowledge the European Synchrotron Radiation Facility for provision of beamtime at beamline ID19 (experiment MA-2183). Constellium C-Tec is thanked for materials supply. Drs. D. Mohr and C. Roth from ETH Zürich are thanked for providing the sample design geometry as well as for scientific discussions.

References

[1] Y. Bao, T. Wierzbicki, On fracture locus in the equivalent strain and stress triaxiality space, International Journal of Mechanical Sciences 46 (1) (2004) 81–98.

[2] J. Papasidero, V. Doquet, D. Mohr, Ductile fracture of aluminum 2024-t351 under proportional and non-proportional multi-axial loading: Bao–wierzbicki results revisited, International Journal of Solids and Structures 69-70 (2015) 459–474.

[3] F. Khameneh, A. Abedini, C. Butcher, Lengthscale effects in optical strain measurement for fracture characterization in simple shear, International Journal of Fracture 232 (2) (2021) 153–180. doi:10.1007/s10704-021-00598-9.

[4] W. Lode, Versuche über den einfluß der mittleren hauptspannung auf das fließen der metalle eisen, kupfer und nickel., Zeitschrift für Physik 36 (1926) 913–939.

[5] A. Abedini, C. Butcher, M. Worswick, Experimental fracture characterisation of an anisotropic magnesium alloy sheet in proportional and non-proportional loading conditions, International Journal of Solids and Structures 144-145 (2018) 1–19.

[6] T. Tancogne-Dejean, C. C. Roth, T. F. Morgeneyer, L. Helfen, D. Mohr, Ductile damage of aa2024-t3 under shear loading: Mechanism analysis through in-situ laminography, Acta Materialia 205 (2021) 116556.

[7] J. Faleskog, I. Barsoum, Tension-torsion fracture experiments–part I: Experiments and a procedure to evaluate the equivalent plastic strain, Int. J. Solids Struct. 50 (25-26) (2013) 4241–4257.

[8] C. C. Roth, D. Mohr, Ductile fracture experiments with locally proportional loading histories, International Journal of Plasticity 79 (2016) 328–354.

[9] K. Miyauchi, A proposal for a planar simple shear test in sheet metals, Scientific Papers RIKEN 81 (1984) 27–42.

[10] E. Till., B. Hackl, Calibration of plasticity and failure models for ahss sheets, In: Proceedings of the International Deep Drawing Research Conference (IDDRG) (2013).

[11] C. C. Roth, D. Mohr, Determining the strain to fracture for simple shear for a wide range of sheet metals, International Journal of Mechanical Sciences 149 (2018) 224 – 240.

[12] A. J. Gross, K. Ravi-Chandar, On the deformation and failure of Al 6061-T6 at low triaxiality evaluated through in situ microscopy, International Journal of Fracture 200 (2016) 185–208.

[13] M. Achouri, G. Germain, P. Dal Santo, D. Saidane, Experimental characterization and numerical modeling of micromechanical damage under different stress states, Materials Design 50 (2013) 207–

222.

[14] C. Landron, E. Maire, J. Adrien, H. Suhonen, P. Cloetens, O. Bouaziz, Non-destructive 3-D reconstruction of the martensitic phase in a dual-phase steel using synchrotron holotomography, Scripta Mat. 66 (12) (2012) 1077–1080.

[15] E. Maire, P. J. Withers, Quantitative X-ray tomography, Int. Mat. Rev. 59 (1) (2014) 1–43.

[16] F. Hannard, T. Pardoen, E. Maire, C. L. Bourlot, R. Mokso, A. Simar, Characterization and micromechanical modelling of microstructural heterogeneity effects on ductile fracture of 6xxx aluminium alloys, Acta Mat. 103 (2016) 558–572.

[17] B. P. Croom, H. Jin, P. J. Noell, B. L. Boyce, X. Li, Collaborative ductile rupture mechanisms of high-purity copper identified by in situ x-ray computed tomography, Acta Materialia 181 (2019) 377–384.

[18] L. Helfen, T. Baumbach, P. Mikulík, D. Kiel, P. Pernot, P. Cloetens, J. Baruchel, High-resolution three-dimensional imaging of flat objects by synchrotron-radiation computed laminography, Applied Physics Letters 86 (7) (2005) 071915.

[19] L. Helfen, T. F. Morgeneyer, F. Xu, M. Mavrogordato, I. Sinclair, B. Schillinger, T. Baumbach, Synchrotron and neutron laminography for three-dimensional imaging of devices and flat material specimens, International Journal of Materials Research 2 (2012) 170–173.

[20] B. Kondori, T. F. Morgeneyer, L. Helfen, A. A. Benzerga, Void growth and coalescence in a magnesium alloy studied by synchrotron radiation laminography, Acta Materialia 155 (2018) 80–94.

[21] M. Shakoor, A. Buljac, J. Neggers, F. Hild, T. F. Morgeneyer, L. Helfen, M. Bernacki, P. O. Bouchard, On the choice of boundary conditions for micromechanical simulations based on 3D imaging, International Journal of Solids and Structures 112 (2017) 83–96. doi:http://dx.doi.org/10.1016/j.ijsolstr.2017.02.018.

[22] C. C. Roth, T. F. Morgeneyer, Y. Cheng, L. Helfen, D. Mohr, Ductile damage mechanism under shear-dominated loading: In-situ tomography experiments on dual phase steel and localization analysis, International Journal of Plasticity 109 (2018) 169 – 192.

[23] X. Kong, L. Helfen, M. Hurst, D. Hänschke, D. Missoum-Benziane, J. Besson, T. Baumbach, T. F. Morgeneyer, 3d in situ study of damage during a 'shear to tension' load path change in an aluminium alloy, Acta Materialia 231 (2022) 117842.

[24] A. J. Tomstad, B. H. Frodal, T. Børvik, O. S. Hopperstad, Influence of particle content on the ductility of extruded non-recrystallized aluminium alloys subjected to shear loading, Materials Science and Engineering: A 850 (2022) 143409.

[25] T. Morgeneyer, L. Helfen, H. Mubarak, F. Hild, 3D Digital Volume Correlation of Synchrotron Radiation Laminography images of ductile crack initiation: An initial feasibility study, Exp. Mech. 53 (4) (2013) 543–556.

[26] T. F. Morgeneyer, T. Taillandier-Thomas, L. Helfen, T. Baumbach, I. Sinclair, S. Roux, F. Hild, In situ 3-d observation of early strain localization during failure of thin al alloy (2198) sheet, Acta Materialia 69 (2014) 78 – 91.

[27] A. Buljac, F. Hild, L. Helfen, T. F. Morgeneyer, On deformation and damage micromechanisms in strong work hardening 2198 t3 aluminium alloy, Acta Materialia 149 (2018) 29 – 45.

[28] T. F. Morgeneyer, M. Khadyko, A. Buljac, L. Helfen, F. Hild, T. Benallal, Ahmed Børvik, O. S. Hopperstad, On crystallographic aspects of heterogeneous plastic flow during ductile tearing: 3D measurements and crystal plasticity simulations for AA7075-T651, International Journal of Plasticity 144 (2021) 103028.

[29] T. Warner, Recently-developed aluminium solutions for aerospace applications, in: Aluminium Alloys 2006 - ICAA10, Vol. 519 of Materials Science Forum, Trans Tech Publications Ltd, 2006, pp. 1271–1278.

[30] A. Buljac, T. Taillandier-Thomas, T. F. Morgeneyer, L. Helfen, S. Roux, F. Hild, Slant strained band development during flat to slant crack transition in aa 2198 t8 sheet: in situ 3d measurements, International Journal of Fracture 200 (1) (2016) 49–62.

[31] T. L. Jolu, T. F. Morgeneyer, A. F. Gourgues-Lorenzon, Effect of joint line remnant on fatigue lifetime of friction stir welded al–cu–li alloy, Science and Technology of Welding and Joining 15 (8) (2010) 694–698.

[32] G. Rousselier, T. Morgeneyer, S. Ren, M. Mazière, S. Forest, Interaction of the Portevin–le Chatelier phenomenon with ductile fracture of a thin aluminum CT specimen: experiments and simulations, Int. J. Fract. 206 (1) (2017) 95–122.

[33] L. Helfen, A. Myagotin, P. Mikulík, P. Pernot, A. Voropaev, M. Elyyan, M. Di Michiel, J. Baruchel, T. Baumbach, On the implementation of computed laminography using synchrotron radiation, Rev. Sci. Instrum. 82 (063702) (2011).

[34] P.-A. Douissard, A. Cecilia, X. Rochet, X. Chapel, T. Martin, T. van de Kamp, L. Helfen, T. Baumbach, L. Luquot, X. Xiao, J. Meinhardt, A. Rack, A versatile indirect detector design for hard X-ray microimaging, Journal of Instrumentation 7 (SEP 2012).

[35] A. Myagotin, A. Voropaev, L. Helfen, D. Hänschke, T. Baumbach, Efficient Volume Reconstruction for Parallel-Beam Computed Laminography by Filtered Backprojection on Multi-Core Clusters, IEEE

Trans. Image Process. 22 (12) (2013) 5348–5361.

[36] M. Vogelgesang, T. Farago, T. F. Morgeneyer, L. Helfen, T. dos Santos Rolo, A. Myagotin, T. Baumbach, Real-time image content based beamline control for smart 4d x-ray imaging, Journal of Synchrotron Radiation 23 (2016) 1254–1263.

[37] T. Faragó, S. Gasilov, I. Emslie, M. Zuber, L. Helfen, M. Vogelgesang, T. Baumbach, *Tofu*: a fast, versatile and user-friendly image processing toolkit for computed tomography, Journal of Synchrotron Radiation 29 (3) (2022) 916–927. doi:10.1107/S160057752200282X.
URL https://doi.org/10.1107/S160057752200282X

[38] J. Chen, Ductile tearing of AA2198 aluminium-lithium sheets for aeronautic application, Phd thesis, ecole Nationale Supérieure des Mines de Paris (2011).

[39] X. Kong, J. Chen, Y. Madi, D. Missoum-Benziane, J. Besson, T. F. Morgeneyer, Plasticity and ductility of anisotropic AA2198 recrystallized in T351 and T851 condition during proportional and non-proportional loading paths: simulations and experiments, accepted in Journal of Theoretical, Computational and Applied Mechanics (2022). doi:10.46298/jtcam.8913.

[40] G. Besnard, F. Hild, S. Roux, "Finite-element" displacement fields analysis from digital images: Application to Portevin-Le Châtelier bands, Exp. Mech. 46 (2006) 789–803.

[41] F. Hild, S. Roux, Comparison of local and global approaches to digital image correlation, Exp. Mech. 52 (9) (2012) 1503–1519.

[42] F. Xu, L. Helfen, T. Baumbach, H. Suhonen, Comparison of image quality in computed laminography and tomography, Opt. Express 20 (2012) 794–806.

[43] S. Roux, F. Hild, P. Viot, D. Bernard, Three dimensional image correlation from X-Ray computed tomography of solid foam, Comp. Part A 39 (8) (2008) 1253–1265.

[44] T. Morgeneyer, T. Taillandier-Thomas, A. Buljac, L. Helfen, F. Hild, On strain and damage interactions during tearing: 3D in situ measurements and simulations for a ductile alloy (AA2139-T3), J. Mech. Phys. Solids 96 (2016) 550–571.

[45] A. Buljac, L. Helfen, F. Hild, T. F. Morgeneyer, Effect of void arrangement on ductile damage mechanisms in nodular graphite cast iron: In situ 3D measurements, Engineering Fracture Mechanics 192 (2018) 242–261.

[46] T. F. Morgeneyer, J. Besson, Flat to slant ductile fracture transition: Tomography examination and simulations using shear-controlled void nucleation, Scripta Materialia 65 (2011) 1002–1005.

[47] C. C. Roth, T. F. Morgeneyer, Y. Cheng, L. Helfen, D. Mohr, Ductile damage mechanism under shear-

dominated loading: In-situ tomography experiments on dual phase steel and localization analysis, International Journal of Plasticity 109 (2018) 169–192.

[48] T. Petit, J. Besson, C. Ritter, K. Colas, L. Helfen, T. F. Morgeneyer, Effect of hardening on toughness captured by stress-based damage nucleation in 6061 aluminum alloy, Acta Materialia 180 (2019) 349–365.